Common defects in diamond lattices as instances of the general T ⊗ ($e + t_2$) Jahn-Teller effect

Gabriela Herrero-Saboya [*] and Layla Martin-Samos

CNR-IOM/Democritos National Simulation Center, Istituto Officina dei Materiali, c/o SISSA, via Bonomea 265, IT-34136 Trieste, Italy

Nicolas Richard

CEA, DAM, DIF, F-91297 Arpajon, France

Anne Hemeryck

LAAS-CNRS, Université de Toulouse, CNRS, F-31031 Toulouse, France

Finding the ground-state configuration of point defects in semiconductors is in general a high-dimensional optimization problem. However, their adiabatic potential energy surfaces (APES) can be described with few effective coordinates by exploiting symmetry arguments within the Jahn-Teller (JT) theoretical framework. In this paper, we propose a general framework, that combines group theory and *ab initio* calculations, to build a full picture of common defects in diamond lattices (vacancies and substitutional impurities) as instances of the general T ⊗ ($e + t_2$) APES. Starting from the original tetrahedral symmetry, we consider all possible JT symmetries and we numerically investigate the shape of the APES by targeting the minimum energy path between equivalent JT distortions taking as examples the vacancy (V) and the metallic impurities Pd, Pt, and Au in crystalline silicon.

I. INTRODUCTION

Recent developments in nanotechnologies have exploited physical properties of systems as small as single point-like defects for novel technological applications. It is the case of quantum sensing devices or quantum computing implementations [1]. From a theoretical point of view, the design of such components requires highly accurate predictive frameworks. However, reliable structural characterization can be challenging even for the simplest defects (e.g., substitutional impurities), since breaking the translational symmetry of the crystal leads to an *a priori* high-dimensional relaxation problem. Indeed, even for commonly studied systems, different *ab initio* optimizations often fail to reach a consensus on the ground-state structure (see e.g., the silicon divacancy [2–13]). Errors in the determination of the ground-state geometry would propagate to the targeted physical properties, such as optically allowed transitions and reaction/diffusion mechanisms. As an alternative strategy to this *blind* search, we propose to guide the *ab initio* characterization through the point symmetries still present in the system, allowing us to reduce the effective dimensionality of the configurational space (Fig. 1). The connection between the highly symmetric pristine crystal and the defect ground state is given by the general Jahn-Teller (JT) theory [14]. This describes the symmetry breaking (SB) in terms of the effective components of the electron-phonon Hamiltonian, identifying the *active* phononic modes, and the consequent compatible lower symmetries. The adiabatic potential energy surfaces (APES) of point defects

are thus dictated by the symmetry loss and therefore, their general shape can be characterized in terms of the preserved symmetries.

Missing atoms (vacancies) or substitutional impurities represent one of the most common cases of symmetry breaking in diamond lattices. As observed experimentally, these centers break the tetrahedral symmetry of the crystal (T_d), resulting in a distorted cubic configuration, with D_{2d}, C_{3v}, or C_{2v} point-group symmetry. For example: From electronic paramagnetic resonance (EPR) spectroscopy, a positive D_{2d} distortion has been reported for the positively charged vacancy (V) in silicon, whereas a positive C_{2v} distortion is assigned to the negatively charged center [15,16]. For the vacancy in diamond, the JT effect $T_d \rightarrow D_{2d}$ was observed to be dynamical [17], resulting in a highly symmetric ground state minimum. In the case of the donor nitrogen (N) in both diamond and silicon, EPR spectroscopy suggests a C_{3v} distortion as the measured ground state [18–20]. Even for the negatively charged palladium (Pd) and platinum (Pt) impurities in silicon, a negative C_{2v} distortion has been observed [21,22]. Among this collection of EPR spectra, one also encounters the unresolved case of neutral gold (Au) in silicon, for which no ground-state geometry could be solidly deduced from the experiment [23,24].

From the theoretical side, vacancies and impurities are often modelled within a defect-oriented study, without considering a global picture for the SB. Throughout this paper, we take a converse approach, treating these common defects as instances of the general problem: the T ⊗ ($e + t_2$) electron-phonon coupling [25]. By exploiting group theory considerations, we first determine the subset of JT symmetries, $T_d \rightarrow D_{2d}$, C_{3v}, C_{2v}, D_2, and C_s. Once the critical points

---

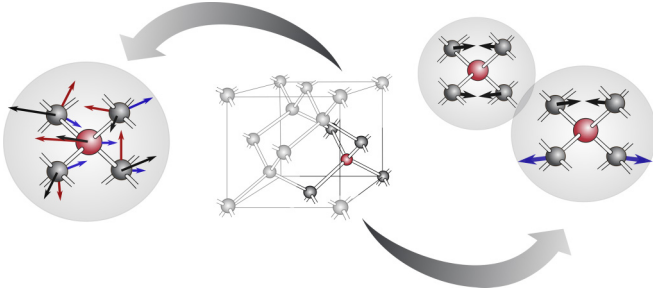*Corresponding author: gherrero@sissa.it

FIG. 1. Structural optimization for a substitutional impurity (red atom) in a diamond lattice: random search (left) vs symmetry-guided relaxation (right).

of the $T \otimes (e + t_2)$ APES are identified, in Sec. III we characterize each of these lower symmetries within a linear combination of atomic orbitals (LCAO) treatment for tetra-coordinated centers, restricted to the center first neighbors. Within such simple toy model, we ground some of the fundamental properties of this family of defects, such as the irreducible representation of the electronic states and the level ordering of their respective eigenvalues. We then numerically investigate the shape of the simple $T \otimes e$ APES for these commonly found cases taking as examples the vacancy and the metallic impurities Pd, Pt, and Au in crystalline silicon (Sec. IV). Finally, in Sec. V we apply such numerical analysis to the general case of the $T \otimes (e + t_2)$ APES. Our state-of-the-art *ab initio* optimization of extremal points is guided by our symmetry-based toy model, allowing us to propose novel and quantitative pictures for the APES.

II. COMPUTATIONAL METHOD

Total energies and forces are obtained within the density functional theory (DFT) framework as implemented in the ABINIT package [26]. The studied defects are embedded in a 215-Si-atoms cell and therefore, the Brillouin zone is only sampled for the Gamma point. We employ the ONCVPSP norm-conserving pseudopotential [27] and the Perdew-Burke-Ernserhof exchange-correlation functional [28]. An energy cutoff for the plane wave basis set of 680, 1306, 1578, and 1578 eV has been employed for the vacancy, Pd, Pt, and Au centers, respectively. Defect configurations at different charge states have been optimized by means of the BFGS algorithm, with a convergence threshold of 1 meV/Å. No symmetry constraints are imposed for structure relaxation. Spin-polarized calculations are employed at charge states $+1$ and -1 ($+2$ and 0 for gold). As commonly implemented in plane-wave codes, ABINIT includes a compensating background charge for non-neutral systems.

The shape of the APES is determined by estimating the MEP between equivalent minima employing the climbing-NEB method [29] as implemented in ABINIT. For all studied paths, the mean total energy threshold between chains of 9 images is inferior to 1 meV.

Many-body corrections are computed on top of the Kohn-Sham energies within the GW approximation (G_0W_0 as implemented in the ABINIT code [26,30]) in order to obtain the defect band structure correctly. Quasiparticle energies for

the vacancy are obtained for a wave function cutoff equal to 680 eV, whereas for the metallic impurities it was set to 1088 eV. We employ the Godby-Needs plasmon-pole model and a cutoff energy of 82 eV to estimate the dielectric matrix. In order to assure convergence of the GW exchange-correlation self-energy, we use a very large ratio of 10:1 empty bands versus occupied bands. Spin-unrestricted calculations are performed for the positive and negative charge states.

III. A TOY MODEL FOR THE TETRAHEDRAL SYMMETRY LOSS IN DIAMOND LATTICES

The tetrahedral symmetry is the natural starting geometry in the diamond lattice. The T_d point-group symmetry consists of the identity E, four rotation axes C_3, three rotation axes C_2, six mirror planes σ_d, and three improper rotations S_4. The consequent character table contains five irreducible representations: A_1, A_2, E, T_1, and T_2. Since any wave function of the symmetric system has to transform according to one of the irreducible representations (Wigner's theorem [31]), the tetrahedral configuration is *a priori* compatible with double (E) and triple (T_1, T_2) electronic degenerate states. In the case of point-like defects in the diamond lattice, vacancies and substitutional impurities break four covalent bonds σ_i, each located at the vertex of a cube [Fig. 2(a)]. The four dangling bonds transform according to the A_1 and T_2 representations, hence spanning the $A_1 + T_2$ defect electronic states. According to the JT theory [14], given a partial occupation of the degenerate electronic term (generally denoted Γ), the system might lower its energy by breaking the original symmetry and consequently, lifting the degeneracy of the electronic states. More importantly, Jahn and Teller demonstrated that the atomic displacements (or normal modes of vibration) lowering the energy of the system could be determined as the irreducible representations of the symmetric direct product of the degenerate electronic term, $[\Gamma^2] - a_1$ (where the a_1 mode simply corresponds to a symmetric displacement or the breathing mode, which leaves the system invariant). Notice that capital letters denote electronic states and lower caps, the phononic modes. In the considered case, $[T_2^2] - a_1 = e + t_2$. The symmetry loss in tetra-coordinated centers in diamond lattices is therefore given by the active JT modes e and t_2, constituting the general $T \otimes (e + t_2)$ JT effect.

Among the nine subgroups of the T_d point group (T, D_{2d}, S_4, C_{3v}, C_{2v}, D_2, C_3, C_2, C_s), we now narrow the symmetries that are compatible with the JT theory, by identifying the ones that are accessible by the e and t_2 modes. As stated in [32], a subgroup is a JT symmetry if the irreducible representation of the active modes in the parental group *contains* the totally symmetric representation (e.g., a_1, a_{1g}, a', etc.) in the lower point group. The T subgroup can therefore be trivially rejected, since $e \rightarrow e$ and $t_2 \rightarrow t$. In the case of the D_{2d} subgroup, $e \rightarrow a_1 + b_1$ and $t_2 \rightarrow b_2 + e$. The D_{2d} symmetry is therefore a plausible JT configuration, which is obtained through an e-type atomic distortion [Fig. 2(b)], constituting the $T \otimes e$ JT effect. Equivalently, the C_{3v} subgroup is JT compatible through a t_2-type deformation, resulting in the $T \otimes t_2$ electron-phonon coupling. If a subgroup of the original symmetry is also a subgroup of a lower JT symmetry (i.e., there is an intermediary group), then the representation of the
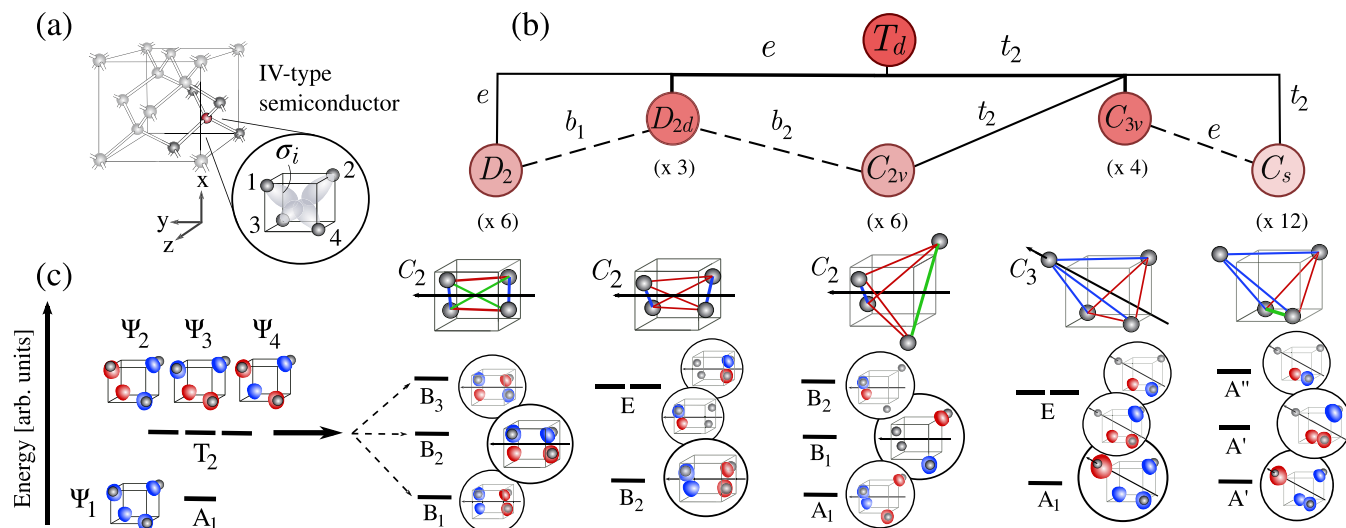
FIG. 2. A simple model for the tetrahedral symmetry loss in diamond lattices. (a) The point-like defect is represented as a red atom embedded in the diamond lattice. The proposed toy model approximates the defect to the center-first neighbors, or atoms 1, 2, 3, and 4, and the defect-related states are estimated as a linear combination of dangling bonds σ_i. (b) Possible JT symmetries lifting the degeneracy of the triplet electronic states T_2 of the tetrahedral configuration. The lower symmetries are connected to the parental group through an atomic deformation of e or t_2 symmetry. For each of the SB mechanisms, the number of equivalent JT configurations resulting from the parental symmetry is indicated in parenthesis. In dotted lines, a second JT effect is represented. These SB processes are triggered by the electronic doublet E, characteristic of the D_{2d} and C_{3v} symmetries. (c) Defect states, energy diagrams, and atomic distortions for the JT symmetries. The splitting and ordering of the levels are estimated within the simple LCAO-based approach. The energy difference between states is qualitatively illustrated. Wave functions Ψ_i are qualitatively depicted according to the following color notation: blue/red regions represent positive/negative contributions. On the left, the energy diagram for the tetrahedral symmetry T_d: the electronic wave function Ψ_1 corresponds to the A_1 representation, which is lower in energy with respect the $\Psi_{2,3,4}$ states constituting the T_2 triplet. On the right, the atomic distortions for the different possible SB mechanisms $T_d \rightarrow D_d$, D_{2d}, C_{2v}, C_{3v}, and C_s, are explicitly shown. Notice that only one of the degenerate JT distortions is shown in each case. The *preserved* symmetry axis for the depicted distortion, described by one of the three original C_2 axes for tetragonal distortions or one of the four C_3 axes for the trigonal configuration, is also indicated. Equal interatomic distances are represented in the same color. For each of the SB mechanisms, a JT energy diagram is shown. The defect-induced wave functions corresponding to the original T_2 states are plotted and they are named according to their irreducible representation. Within our toy model, the highly symmetric Ψ_1 state remains invariant and it presents a A_1 representation for all the JT processes. Notice this state is always the lowest in energy and it is excluded from the energy diagrams for the JT distortions.

deformation mode for the intermediate group has to create the symmetric representation in its subgroup. The D_2 subgroup is JT active through two atomic distortions with e symmetry, since,

$$
\begin{array}{cccc}
T_d & D_{2d} & D_2 \\
e & \rightarrow & a_1 + b_1 & \rightarrow & a + a.
\end{array}
\tag{1}
$$

On the contrary, the S_4 symmetry is not a JT configuration, since the $a_1 + b_1$ representations of the D_{2d} intermediate group transform as $a + b$. Applying analogous arguments, the C_2 and C_3 symmetries are discarded as JT symmetries, whereas the C_{2v} and C_s subgroups break the tetrahedral configuration through t_2 modes [Fig. 2(b)].

From the group theory analysis, the five candidates to lower the energy of the tetrahedral group are narrowed to: D_{2d}, D_2, C_{3v}, C_{2v}, and C_s. In the case of an *actual* physical system, one can further reduce the symmetry of the ground state minimum by considering the occupation of the electronic terms. As a standard principle, the system is going to preserve the largest number of symmetry elements as long as the localized electrons are occupying singlet states. Among the candidate subgroups, the D_{2d} and C_{3v} configurations present the largest number of symmetry elements. For these symmetry breakings,

the T_2 states are lifted as B_2+E and A_1+E respectively, which guarantees that up to two electrons can be accommodated on singlet states. If the electronic occupation is further increased, the electronic doublet E becomes partially occupied and a *second* JT distortion is required to lift the degeneracy. The E doublet in the D_{2d} symmetry can be broken through b_1 and b_2 modes ($[E^2] - a_1 = b_1 + b_2$), resulting respectively on a D_2 and C_{2v} configuration. The b_1 mode is of e type in the parental T_d configuration, whereas the b_2 mode corresponds to an original t_2 deformation. The C_{2v} symmetry is therefore a special case, since the T_d configuration might fall into such JT symmetry through a pure t_2 deformation or by a combination of e and t_2 modes [Fig. 2(b)], representing the $T \otimes (e + t_2)$ effect. In the case of the C_{3v} group ($[E^2] - a_1 = e$), one single JT symmetry is predicted: the C_s group. These second JT effects are represented with dotted lines in the diagram of symmetry in Fig. 2(b).

We now ground the consistent study of the tetrahedral symmetry breaking through a simple toy model, based on the center first neighbors and corresponding dangling bonds [host atoms 1, 2, 3, and 4 and broken bonds $\{\sigma_i\}$ in Fig. 2(a)]. Within such general framework, the effective atomic displacements (or the normal modes of vibration) are described

by a system of four atoms, here referred to as the $N = 4$ system. Regarding the electronic terms, our defect-induced wave functions are obtained as a linear combination of the four broken bonds and the energy-level ordering of such states is determined from a simple two-center Hamiltonian. Even if similar LCAO treatments have been previously proposed for specific JT distortions (e.g., the well-known vacancy model for a missing atom in silicon [15,16]), here we retain a global perspective, explicitly covering all the possible JT effects arising from the tetrahedral symmetry. In the following, we consider the most plausible SB mechanisms for a given electronic occupation, explicitly describing the JT distortions for the $N = 4$ system, the irreducible representations of the defect-induced states and their corresponding energy-level ordering.

Starting from the precursor symmetry, the defect-induced states are defined as the electronic wave functions $\Psi_{1,2,3,4}$ in Fig. 2(c). The highly symmetric Ψ_1 state, with irreducible representation A_1, is lower in energy with respect to the degenerate states $\Psi_{2,3,4}$, constituting the triplet state T_2. Let us now consider an electronic occupation of the T_2 states equal one (or two): $T_2^{\uparrow}$ (or $T_2^{\uparrow\downarrow}$). In order to preserve the largest number of symmetry elements, the system falls into either the D_{2d} or the C_{3v} configurations. We first consider the $T_d \rightarrow D_{2d}$ mechanism, for which one of the three C_2 axes of the parental group is preserved, resulting on three equivalent D_{2d} distortions.

In this paper, we take the three C_2 axes corresponding to the Cartesian axes: D_{2d}^x, D_{2d}^y, and D_{2d}^z. In Fig. 2(c), we explicitly show the D_{2d}^y distortion, for which the six degenerate distances between the four atoms are split by forming two pairs of atoms, decreasing two distances (d_{13}, d_{24}) with respect the remaining four (d_{12}, d_{24}, d_{13}, d_{34}). For any of the equivalent D_{2d} distortions, the degeneracy of the T_2 states is broken. In particular, for the depicted D_{2d}^y configuration and within the considered approximation, the Ψ_2 state with B_2 representation is favored over the E doublet, given by a linear combination of Ψ_3 and Ψ_4. For an electronic occupation equal one, the electronic configuration is therefore: $B_2^{\uparrow}E$. In the case of the $T_d \rightarrow C_{3v}$ SB, the tetrahedral symmetry falls into one of the fourfold trigonal distortions, each defined by a C_3 axis intersecting one of the four host atoms. In Fig. 2(c) (right), the C_3 axis passes through atom 1, lifting the degeneracy of the interatomic distances by increasing the distance between atom 1 and the remaining three. The Ψ_2 state presents a A_1 symmetry, whereas states $\Psi_{3,4}$ constitute the doublet E. The original $T_2^{\uparrow}$ electronic configuration therefore becomes, $A_1^{\uparrow}E$.

If the original T_2 states present an electronic occupation equal three (or more), $T_2^{\uparrow\downarrow\uparrow}$, the system falls into either a sixfold C_{2v} or D_2 distortions or into a twelvefold C_s configuration (Fig. 2). For the sake of conciseness, in the following we only treat the higher order symmetries C_{2v} and D_2, but an analogous analysis can be made for the C_s group. The C_{2v} distortion, contained in the D_{2d} group, further breaks the symmetry by lifting the degenerate distances between the *paired* atoms, resulting in a configuration characterized by three distances. For each of the degenerate D_{2d} geometries, two C_{2v} distortions can coexist given a C_2 symmetry axis. In

Fig. 2(c), one of the C_{2v}^y distortions is plotted, characterized by a distance d_{13} smaller than d_{24}: the $C_{2v}^{y\,>}$ configuration. If such inequality were to be inverted, the distortion would be denoted by $C_{2v}^{y\,<}$. For any of the six equivalent distortions, the degeneracy of the electronic triplet is completely lifted, resulting in three singlets: A_1, B_1, and B_2. Within this model and for the depicted C_{2v} configuration, the A_1 representation is the lowest in energy and it corresponds to the Ψ_2 state. The remaining two singlets can be written as a linear combination of the original $\Psi_{3,4}$ states, as represented in Fig. 2 ($B_1 \sim \Psi_3 + \Psi_4$ and $B_2 \sim \Psi_3 - \Psi_4$). If on the contrary the system falls into a D_2 distortion, the system is characterized by three twofold degenerate distances. Visualizing the D_2 configuration again as a distorted D_{2d} configuration, the symmetry is further broken by rotating the two paired of atoms in opposite senses. As depicted in Fig. 2 for a precursor D_{2d}^y symmetry: the paired of atoms 13 is rotated clockwise, whereas the pair 24 moves counterclockwise, decreasing the distances d_{12} and d_{34} over the remaining two (d_{14} and d_{23}). Similarly to the C_{2v} distortions, two D_2 configurations coexist for a given C_2 axis. The second D_2^y distortion can simply be deduced by rotating the paired atoms in the opposite senses.

In addition to this description, for each of the JT symmetries, two opposite senses of distortion are possible, duplicating the number of plausible extremal points of the APES. For the $T_d \rightarrow D_{2d}$ SB, an opposite sense of the D_{2d}^y distortion also lifts the degeneracy of the triplet electronic states, lowering the E doublet below the singlet A_1. Such configuration is given by the same set of equivalent interatomic distances, but the separation between the paired atoms is now increased. The consequent negative $C_{2v}^{y\,>}$ distortion is given by further differentiating such *large* paired distances. This new configuration also inverts the level ordering, favoring the B_1 and B_2 states over the A_1 singlet. Anticipating the coexistence of both senses of distortion in a given JT model, here we denote as the positive sense of distortion the configurations represented in Fig. 2, and the negative distortion their corresponding opposite senses.

The group theory analysis presented in this section allows to determine the set of JT symmetries compatible with the triplet states T_2, characteristic of the tetrahedral geometry. Among the five candidates, the *preferred* JT distortion can be further narrowed by acknowledging the splitting of the T_2 states into a singlet and a doublet (for the D_{2d} and C_{3v} symmetries) or three singlets (in the case of the D_2 and C_{2v} symmetries) and considering a specific electronic occupation, as exemplified with the toy model. For a given electronic occupation, one is however not capable of predicting the most stable JT symmetry without explicitly solving the electronic interaction (for example, D_{2d} or C_{3v} for the electronic configuration $T_2^{\uparrow}$). In the following sections, we therefore consider specific centers in silicon inducing triplet states and we solve the electronic Coulomb term by performing *ab initio* calculations. The simple vacancy and the substitutional impurities Pd, Pt, and Au allow us to explicitly consider electronic occupations equal one, two, and three of the triplet electronic states. Our computational results are thus validated with the simple symmetry-based toy model and contextualized in the general JT theory.
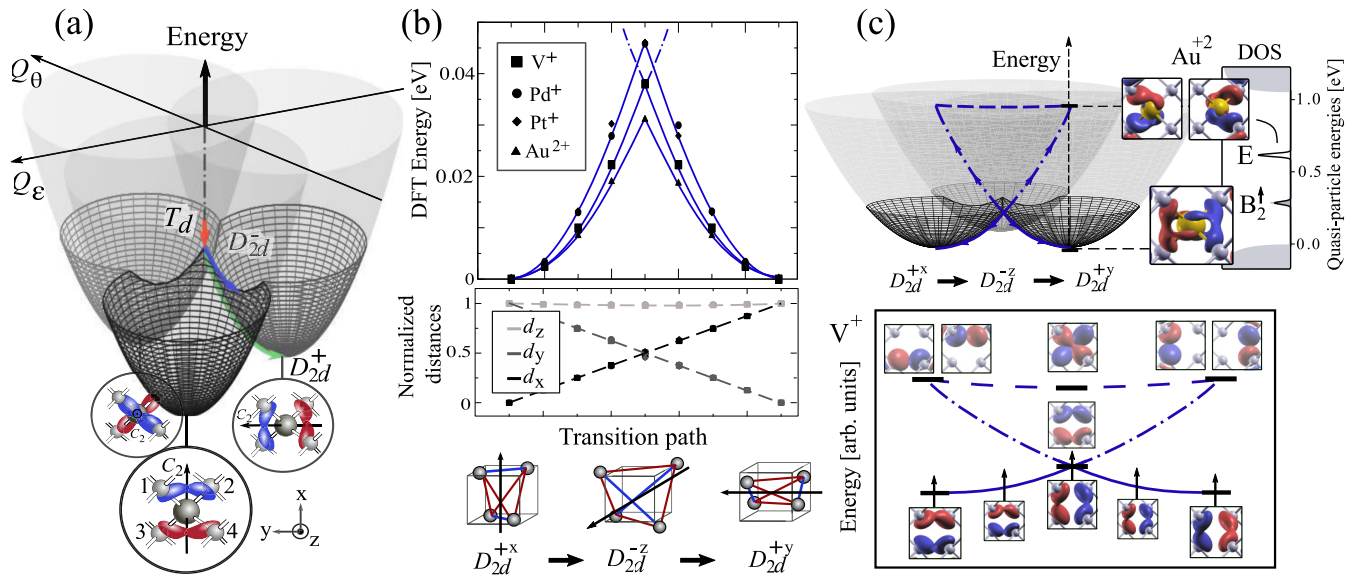
FIG. 3. Full theoretical picture of the $T_d \rightarrow D_{2d}$ SB in silicon. (a) General APES for the T$\otimes e$ problem constituted by three paraboloids, whose minima correspond to the three equivalent D_{2d}^+ distortions oriented along the Cartesian axes. The equivalent minima are represented for the Pt impurity and its highest occupied defect state (the B_2 state). The intersection of the three surfaces for $Q_\epsilon = Q_\theta = 0$ corresponds to the tetrahedral symmetry, T_d. The black grid represents the mixed electronic manifold sampled by a ground state theory. (b) A DFT study of the reorientation process: NEB calculations between equivalent distortions D_{2d}^{+x} and D_{2d}^{+y} for V^+, Pd^+, Pt^+, and Au^{2+}. In the upper panel, the DFT energy along the MEP is plotted. In the lower panel, the normalized interatomic distances, $d_i = \frac{d_i - d_{min}}{|d_{max} - d_{min}|}$, throughout the transition path are shown. The six interatomic distances are denoted as followed: $d_{12} = d_{34} := d_x$, $d_{13} = d_{24} := d_y$, and $d_{14} = d_{23} := d_z$. The cusp of the transition therefore corresponds to a negative D_{2d}^{-z} distortion. (c) Defect-induced Kohn-Sham eigenfunctions as the electronic wave functions of the $T_d \rightarrow D_{2d}$ mechanism. In the upper panel, the quasiparticle (QP) energy DOS within the GW approximation is plotted for Au at $+2$ charge state. The bulk states are represented in grey, whereas the defect states are indicated by their irreducible representation: B_2 and E. In the lower panel, the lack of variation of the defect states along the reorientation process, $D_{2d}^{+,x} \rightarrow D_{2d}^{-z} \rightarrow D_{2d}^{+,y}$, is represented.

IV. THE T $\otimes e$ APES: SYMMETRY PROTECTED TRANSITIONS BETWEEN EQUIVALENT D_{2d} DISTORTIONS

In the current section, we consider the simple vacancy (V) and the substitutional impurities Pd, Pt, and Au in silicon at charge states $+1$ and 0 ($+2$ and $+1$ for gold), which correspond to electronic occupations equal one or two of the triplet states, $T_2^\uparrow$ or $T_2^{\uparrow\downarrow}$. Given this electronic occupation (see Sec. III), the tetrahedral system preserves the largest number of symmetry elements by falling into either a D_{2d} or C_{3v} symmetries. Our *ab initio* calculations find as the minimum of the energy surface a positive D_{2d} distortion (denoted D_{2d}^+) for all the considered centers. As anticipated by the simple toy model, the JT distortions are mainly described by the center first neighbors (or atoms 1, 2, 3, and 4). We can thus assume that the exploration of the APES can be carried out on the subspace of atomic displacements described by the $N = 4$ system, as postulated in the precedent section. Previous first-principles calculations have already proposed such ground-state geometry for the vacancy in silicon [33–38], whereas only in the case of substitutional gold a D_{2d}-like configuration has been earlier described [39]. The scope of our analysis is however not to target individual ground state geometries, but to contextualize the numerically optimized D_{2d}^+ geometry in the general JT theory.

Once the JT mechanism is established, we exploit the model for the T $\otimes e$ APES proposed in [25] to guide the

ab initio exploration of the configurational space. To first order of the electron-phonon coupling [25], the energy surface was found to have three equivalent minima in the subspace given by two effective atomic displacements or normal modes e, often denoted as the Q_ϵ and Q_θ atomic displacements. The three degenerate D_{2d}^+ minima correspond to three paraboloids whose relative positions are represented in Fig. 3(a). Notice that each of the equivalent D_{2d}^+ distortions, defined with respect one of the Cartesian axis, are explicitly shown for the Pt impurity in Fig. 3(a). In the subspace of e-type atomic displacements, the highly symmetric configuration T_d is located at the intersection of the three surfaces, given by $Q_\epsilon = Q_\theta = 0$. Within such approximation, the transitions between the degenerate minima are symmetry protected, since each of the wells is by construction described by a different electronic manifold. The transition between D_{2d} distortions is therefore not continuous, but it is characterized by a *cusp*. In any realistic system, further orders of perturbation might however become relevant, opening an avoided level crossing along the parabola defined by the intersection of two paraboloids. Such intersection, equidistant from the wells in the Q_ϵ-Q_θ plane, is here postulated to present an opposite sense of the JT distortion or to correspond to the D_{2d}^- configuration [marked with a blue line in Fig. 3(a)].

We now move to the *ab initio* exploration of the energy surface, taking as starting points the highly symmetric paths identified in the simple model for the T$\otimes e$ APES. Since

DFT is a ground state theory, the sampling of the APES is restricted to the lowest electronic manifold, which is represented as a black mesh in Fig. 3(a). In particular, we target the minimum energy path (MEP) between equivalent D_{2d} distortions for all the studied centers at positive charge state (+2 for Au). As represented in Fig. 3(b), considering the particular case $D_{2d}^{+x} \to D_{2d}^{+y}$: the MEPs between equivalent distortions present a cusp, strongly indicating the existence of a level crossing or a relatively small avoided level crossing (as predicted by the simple T $\otimes e$ model). In order to obtain more information regarding the transition path, we analyze the change of interatomic distances along the MEP. Exploiting the symmetry of the transition path, the set of six distances is fully described by three single values, since: $d_{12} = d_{34} = d_x$, $d_{13} = d_{24} = d_y$, and $d_{14} = d_{23} = d_z$, as it is schematised in Fig. 3(a) (bottom). As represented in Fig. 3(b), the behavior of the distances along the MEP reveals three D_{2d} configurations, two of them with a positive sense of distortion (e.g., $d_x < d_y = d_z$ for the initial D_{2d}^{+x} configuration) and a negative D_{2d} distortion with unpaired distances d_z. The *ab initio* exploration of the APES thus finds that the cusp characterizing the reorientation process presents a D_{2d}^- distortion, coherently with symmetry considerations. Moreover, the change of the six interatomic distances along the transition path [Fig. 3(b)] reveals that the MEP actually corresponds to a simple linear interpolation between the two wells, in alignment with the general model of the APES. Given that equivalent plots are obtained for all the centers at neutral charge state (+1 for Au), we can conclude that our first-principles calculations on specific centers are consistent with a transferable theoretical picture provided by the general JT theory.

A final statement regarding the shape of the APES can be made by further analyzing the defect-induced electronic wave functions through the reorientation process. If the defect states remain invariant along the studied MEP, the cusp corresponds to a level crossing of two different electronic wave functions. On the contrary, if the electronic wave function is allowed to gradually change through the transition, the reorientation process is described by a single manifold and the cusp is an avoided level crossing. In this work, we approximate the electronic wave functions by the real space projection of the Kohn-Sham eigenfunctions. The four defect-states A_1, B_2, and E (a doublet) predicted by the toy model, only three appear as disentangled eigenfunctions with respect the bulk states [defects states B_2 and E, plotted for Au at +2 charge state in Fig. 3(c)]. Moreover, as predicted by the toy model (JT energy diagram in Fig. 2), the quasiparticle (QP) energy associated to the B_2 state is lower in energy with respect to the doublet E [QP energy density of states (DOS) within the GW approximation for the gold impurity in Fig. 3(c)].

At charge state +1 (+2 for the Au impurity), the unpaired electron is localized at the singlet B_2, positioned within the silicon band gap for all the studied centers. Due to the strong localization of the B_2 and E states, they can be easily linked to the general T $\otimes e$ model: The wave function corresponding to the localized electron is given by one of the three wells of the T $\otimes e$ APES, whereas the empty doublet is given by the intersection of the remaining two paraboloids [Fig. 3(c)]. The energy variation of these electronic states along the path between two wells is thus indicated by the surface of the

TABLE I. Activation energies between equivalent D_{2d} distortions for Pd, Pt, Au, and the vacancy at electronic occupations $B_2^\uparrow$ and $B_2^{\uparrow\downarrow}$. Measured values [16] and previous estimated barriers [34,36] are also shown. All values are given in eV.

Trap occ.	Pd	Pt	Au		V	
$B_2^\uparrow$	0.05	0.05	0.03	0.04	0.013 [16]	0.05 [34]
$B_2^{\uparrow\downarrow}$	0.16	0.15	0.10	0.20	0.23 [16]	0.32 [36], 0.20 [34]

three intersecting paraboloids, as represented in blue lines in Fig. 3(c). Taking as an example the V^+ center, the ground state remains invariant as the B_2 state of x symmetry until the intersection, where it is forced to change into a different B_2 state along the y axis, characteristic of a D_{2d}^{+y}. The electronic wave functions are thus invariant within the Q_ϵ-Q_θ plane, regardless of the atomic deformation. We have therefore shown that the three JT distortions are symmetry protected, each of them characterized by a different electronic wave function. We remark that the difference between the unoccupied wave functions for the positive distortions with respect to the negative configuration is a mere choice of the diagonalization algorithm, since both sets of E eigenfunctions span the same degenerate subspace. Moreover, in the case of the D_{2d}^- distortion, the degeneracy of the doublet E is slightly lifted in our *ab initio* calculations due to the difficulty of accurately describing the cusp of the transition theoretically given by the exact degeneracy of the distances d_x and d_y in the plot 3(b). We remark that no smearing of the electronic occupation is considered and no symmetry constraint is imposed to the estimated path. Since equivalent tendencies are obtained for $V^{+,0}$, $Pd^{+,0}$, $Pt^{+,0}$, and $Au^{+,+2}$ in silicon, we show that the DFT sampling of the APES for all the centers follows the simple general T $\otimes e$ model.

To conclude, we emphasize that even if our model for the T $\otimes e$ energy surface might look similar to the warped APES corresponding to the well-investigated E $\otimes e$ problem [25], the three equivalent minima in that case are described by a single-electronic manifold, whereas in the current problem they belong to different electronic wave functions. The observed reorientation between equivalent distortions for the simple vacancy can thus not be explained by continuous jumps between the minima of the APES, as it was the case for the E center in silicon [40]. In other words, the static description of the APES described here is not sufficient to predict the symmetry-protected transitions, since the global model would require the inclusion of dynamical effects (e.g., a perturbation of the lattice in the vicinity of the center, an electronic de-excitation thorough photons, the energy dissipation by lattice phonons, etc.). In Table I we however show that the dynamical corrections are small, since our DFT estimated activation energies are in close agreement with the measured reorientation barriers. Among the previous *ab initio* values, we remark that in the case of [34], the activation energies at both charge states were given without further investigating the general shape of the APES, neglecting the prohibited character of the transition. In the case of [36], the saddle point of the transition was presented to have a C_{3v} geometry, in strong disagreement with our model for the APES, restricted to the
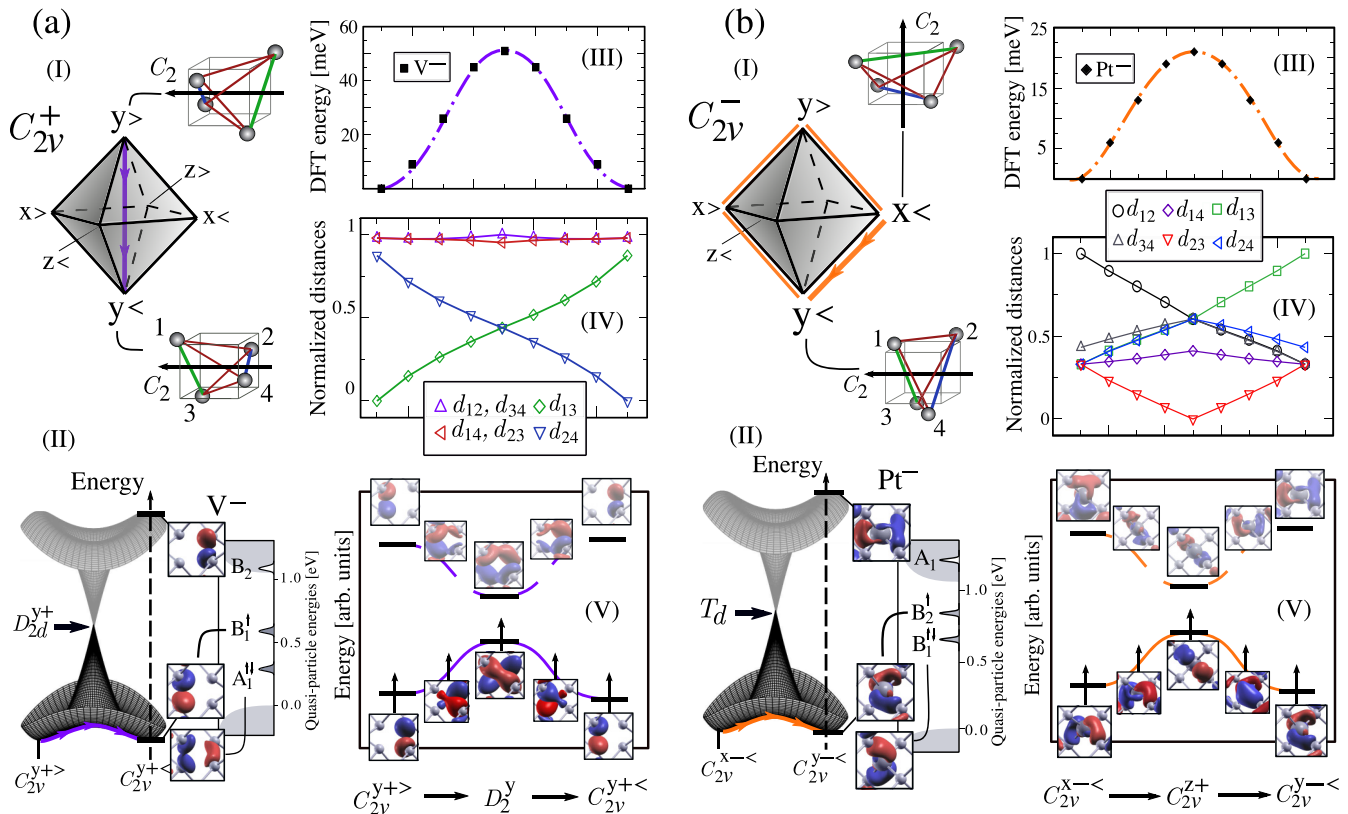
FIG. 4. Comprehensive picture for the $T_d \to C_{2v}$ SB mechanism in silicon. The six equivalent C_{2v} distortions are positioned at the vertexes of an octahedron, following the notation introduced in III. (a) The C_2-restricted transitions. (I) The C_2-restricted path is represented in purple for positive C_{2v} distortions. The initial and final configurations of the transition between C_{2v}^{y+} distortions are represented for the center first neighbors or atoms 1, 2, 3, and 4. (II) The proposed APES for the sampled space is represented, where the two minima are assigned to the $C_{2v}^{y+>}$ and $C_{2v}^{y+<}$ distortions. The lowest electronic manifold is identified with the B_1 state of the negative vacancy, whereas the highest manifold corresponds to the B_2 state. The quasiparticle density of states shows the position of those electronic states and the A_1 defect level within the silicon band gap. [(III)–(V)] A DFT study of the reorientation process $C_{2v}^{y+>} \to C_{2v}^{y+<}$ is shown. (III) The DFT total energy along the MEP. (IV) The normalized interatomic distances, $d_{ij} = \frac{d_{ij} - d_{\min}}{|d_{\max} - d_{\min}|}$ along the transition path. The distances d_{ij} correspond to the schematic representations for the $N = 4$ system on the left. The saddle point of the transition corresponds to a D_2^y configuration. (V) The smooth variation of the two highest defect states along the transition path $C_{2v}^{y+>} \to D_2^y \to C_{2v}^{y+<}$ is shown. (b) The C_2-unrestricted transitions . (I) The C_2-unrestricted path is shown in orange for the negative C_{2v} distortions. The initial and final configurations of the transition between $C_{2v}^{x-<}$ and $C_{2v}^{y-<}$ distortions are represented. (II) The model for the APES restricted to the sampled space is shown. The lowest electronic manifold is identified with the B_2 state of the negative Pt impurity, whereas the highest manifold corresponds to the A_1 state. The quasiparticle density of states reveals that the fully occupied B_1 state and the partially occupied B_2 state lay in the band gap, whereas the A_1 state is located in the conduction band. [(III)–(V)] A DFT study of the reorientation process $C_{2v}^{x-<} \to C_{2v}^{y-<}$ is represented. (III) The DFT total energy along the computed MEP. (IV) The normalized interatomic distances along the transition path, where the distances d_{ij} correspond to the schematic representations for the $N = 4$ system on the left. The saddle point of the transition is identified with a C_{2v}^{z+} configuration. (V) The smooth variation of the two highest defect states along the transition path $C_{2v}^{x-<} \to C_{2v}^{z+} \to C_{2v}^{y-<}$ is schematically represented.

Q_ϵ-Q_θ plane. We hence conclude with the restatement that a strong symmetry-based analysis of the APES is fundamental for a meaningful *ab initio* characterization of the center finite-temperature dynamics.

V. THE $T \otimes (e + t_2)$ APES: C_{2v} AND D_2 DISTORTIONS AS EXTREMAL POINTS

We finally consider triply occupied T_2 states, $T_2^{\uparrow\downarrow\uparrow}$, which correspond to the negative charge state of the vacancy and the metallic impurities Pd and Pt and the neutral Au. According to previous group theory considerations (Sec. III), the $T_2^{\uparrow\downarrow\uparrow}$ electronic configuration might result into the SBs $T_d \to D_2, C_{2v}, C_s$. Our *ab initio* calculations in crystalline

silicon find as global minima of the energy surfaces a C_{2v}^+ for V$^-$ and C_{2v}^- for Pd$^-$ and Pt$^-$. Analogously to the D_{2d} model, the JT distortions are described by the centers first Si neighbors, in agreement with the toy model. For the metallic impurities exhibiting negative C_{2v} distortions, we report a displacement from their perfect substitutional site along the C_2 symmetry axis and in the direction of the second largest interatomic-distance (for $C_{2v}^{y>}$ with $d_{13} < d_{24}$, Pd and Pt move towards Si atoms 2, 4, Fig. 4). In the case of the Au^0 center, isoelectronic to Pt$^-$, the estimated ground state geometry however presents a D_2 symmetry. This result remains compatible with the JT model, since the D_2 subgroup is predicted to be a JT symmetry (Sec. III). Indeed, given the common D_{2d} ground state geometry for occupations one and two of

the original T_2 states (precedent section), these calculations confirm that the degeneracy of the electronic doublet E can be lifted by the D_2 or C_{2v} symmetries. For an electronic occupation of the T_2 states equal three, our model therefore predicts that the the precursor T_d symmetry falls into either sixfold C_{2v} or D_2 distortions. From previous *ab initio* calculations [33,37,38], only the positive C_{2v} symmetry has been assigned to the negatively charged vacancy, overlooking the implications of negative C_{2v} distortions in the general theory. In the case of neutral gold, a D_2-like distortion was previously proposed [39], without further stating the role of such symmetry in the overall JT model. From a second study [41], a C_{2v} distortion was suggested for Au^0, describing its displacement from the ideal substitutional position. Similarly to the analysis carried out in the precedent section, our computational effort is not limited to characterising the ground state symmetries, but to provide a comprehensive sampling of the APES. In particular, we describe the C_{2v} energy surfaces for the negative centers V, Pd, and Pt. Within such JT model, we however identify the relevant role of the D_2 distortions in the overall picture of the APES.

From group theory considerations (Sec. III), we established that the C_{2v} symmetry corresponds to the SB of the T_d configuration through both e and t_2 distortions, constituting the $T \otimes (e + t_2)$ coupling. A complete model for the $T_d \rightarrow C_{2v}$ mechanism should therefore be developed in the subspace defined by five JT active modes, which are commonly denoted as: Q_ϵ, Q_θ, Q_η, Q_ζ, and Q_ξ. Within such global picture, trigonal, tetragonal, and orthorhombic distortions coexist and are described as minima and saddle points of the energy surface [25]. Anticipating the complexity of sampling this entire subspace [25], we restrict the analysis of the APES to two different symmetry-imposed paths. These transition paths correspond to the two possible reorientation mechanisms between equivalent C_{2v} distortions. As represented in Fig. 4, such mechanisms can be easily conceived by positioning the six minima of the APES on the vertexes of a regular octahedron. As represented for the positive distortion [Fig. 4(a)] and the negative distortion [Fig. 4(b)], we force C_{2v} distortions with respect to the same C_2 symmetry axis (e.g., $C_{2v}^{y>}$ and $C_{2v}^{y<}$) to be placed on opposite vertexes of the polyhedron. The small reorientations between C_{2v} distortions with respect to the same C_2 axis ($> \leftrightarrow <$) are thus represented by paths between opposite vertexes, as depicted with a purple line for the C_{2v}^+ case in Fig. 4(a)(I). The transition between JT distortions with respect to different C_2 axis are represented by the edges of the octahedron, as shown with an orange path for the C_{2v}^- case in Fig. 4(b)(I).

Let us start with the simple case of the small reorientations between C_{2v} distortions with respect to the same C_2 axis: the C_2-restricted transition [Fig. 4(a)]. The computed MEP for the negative vacancy reveals a continuous transition between equivalent JT distortions, indicating that the transition path is not symmetry protected. Aiming for a full characterization of the path, we plot the normalized interatomic distances between atoms 1, 2, 3, and 4 along the computed MEP between C_{2v}^y distortions. As shown in Fig. 4(a)(IV), from the degeneracy of the six interatomic distances one can deduce the nature of the saddle point. For both minima, the set of six

distances have two nondegenerate ones (d_{13} and d_{24}), whose values are exchanged from the initial to the final configuration. At the saddle point, the degeneracy of the four remaining distances is lifted, obtaining three sets of twofold degenerate distances: a D_2 distortion. This saddle point is however degenerate, since two D_2^y configurations are available. For each of the three transitions along the Cartesian axes, two MEPs are thus available, corresponding to the two equivalent D_2^x, D_2^y, and D_2^z distortions. We further investigate the symmetry character of the small reorientation process by plotting the real-space projection of the KS eigenfunctions corresponding to the defect-related states along the MEP [Fig. 4(a)(V)]. In this case, the localized wave functions continuously evolve from the eigenstates of a C_{2v} distortion (states A_1, B_1, and B_2 in Fig. 2) to the ones of a D_2 symmetry (B_1, B_2, and B_3 in Fig. 2). The shape of the APES can thus be identified with one single-electronic manifold, which corresponds to the highest occupied state (or the B_1 state). The lowest unoccupied defect state corresponds to the B_2 state, which is represented by a second electronic manifold. These manifolds become degenerate (electronic doublet E) by imposing the higher symmetry D_{2d}^{y+}, constituting a conical intersection or level crossing. The fully occupied A_1 state is lower in energy and remains invariant within the sampled space of atomic displacements. To conclude, we remark that an equivalent model for the small reorientation between equivalent C_{2v}^- distortions for Pd^- and Pt^- remains valid. For this sense of distortion, the defect-related levels are inverted and the electronic occupation is thus: $B_1^{\uparrow\downarrow} B_2^\uparrow$. The shape of the APES in this case is dictated by the highest occupied state: the B_2 state. Moreover, throughout the small reorientation process between C_{2v}^y distortions, the metallic impurity moves from its interstitial position closer to atoms 2, 4, to a substitutional position at the saddle point, before going back to an interstitial position approaching atoms 1, 3.

We now consider the reorientation mechanism between equivalent C_{2v} distortions with respect to different C_2 axis: the C_2-unrestricted process. As represented in Fig. 4(b) for the $C_{2v}^{x-<} \rightarrow C_{2v}^{y-<}$ process for Pt, this MEP does also correspond to a continuous transition. Similarly to previous investigations, we plot the change of interatomic distances along the studied path in Fig. 4(b)(IV). In this case, all distances are non-degenerate except for the initial, final and saddle point configurations. Due to the change of C_2 axis along the transition, the negative C_{2v} distortions present different nondegenerate distances (d_{12} and d_{34} for $C_{2v}^{x<}$, and d_{13} and d_{24} for $C_{2v}^{y<}$). The saddle point also presents a C_{2v} symmetry, with yet another set of nondegenerate distances (d_{14} and d_{23}). For this defect configuration, such distances are however smaller than the remaining four, constituting a positive C_{2v} distortion. Even if the transition $C_{2v}^{x-} \rightarrow C_{2v}^{z+} \rightarrow C_{2v}^{y-}$ seems analogous to the $D_{2d}^{x+} \rightarrow D_{2d}^{z-} \rightarrow D_{2d}^{y+}$ process discussed in Sec. IV, we remark that in this case the transition is not symmetry protected, as revealed by the absence of cusp in the total energy plot and the continuous transformation of the defect-related wave functions along the path [Fig. 4(b)(V)]. Moreover, given the multiplicity of the C_{2v} distortions, two possible reorientation paths can be conceived due to the degeneracy of the C_{2v}^{z+} distortion. Each of the edges of the octahedron is thus doubly

TABLE II. Activation energies between equivalent C_{2v} distortions for the two types of reorientation for Pd, Pt, and the vacancy at negative charge state. Experimental values are included for the vacancy [16]. All values are given in eV.

Reorientation process	Pd	Pt	V	
C_2-restricted	0.007	0.007	0.051	0.008 [16]
C_2-unrestricted	0.023	0.021	0.116	0.072 [16]

degenerate and the reorientation process can either happen left or right around the *Mexican hat* energy surface [Fig. 4(b)(II)]. An equivalent model is proposed for the reorientation of the negative vacancy, for which the sense of distortion for minima and saddle points of the APES is inverted.

To summarize, we have proposed novel transition paths between equivalent C_{2v} distortions, consistently sampling a subspace of the general $T \otimes (e + t_2)$ problem. We emphasize that the sampled APES corresponds to a single electronic manifold, contrary to the above discussed D_{2d} model. In this case, the warped APES proposed for the reorientation process with unrestricted C_2 axis certainly looks similar to the $E \otimes e$ model for the precursor C_{3v} distortion. We however remark that the plotted energy surfaces are restricted to a subspace of atomic displacements $\{Q\}$ and hence, they do not correspond to the global APES. On the other hand and to the best of our knowledge, only in the context of the $Cr(CO)_6$ compound the MEP between equivalent C_{2v} distortions has been previously investigated [42]. In such work, the saddle point of C_2-unrestricted transitions were postulated to present a C_s symmetry, in contrast with our proposed model. For the selected centers in silicon, we did also estimate a transition path whose saddle point presented a lower C_s symmetry, which did not however correspond to the MEP. Our proposed MEPs for both reorientation processes between equivalent C_{2v} distortions present saddle points with the same symmetry order ($n = 4$) as the minima. Such example explicitly supports the need to guide the *ab initio* characterization by symmetry arguments, especially when exploring APES with a large number of degrees of freedom.

The activation energies obtained for both investigated mechanisms are collected in Table II. As expected, the barrier of the C_2-restricted mechanism is systematically lower with respect to the C_2-unrestricted reorientation process. In the case of the vacancy, both reorientation barriers were obtained by stress-alignment EPR studies [16]. For these cases, we overestimate the measured activation energies by ~ 40 meV. This energy difference is however consistent with similar absolute errors reported in the context of *ab initio* calculations of defects in semiconductors. In the case of the metallic impurities, the low barrier for the C_2-restricted mechanism is in alignment with the observed reorientation between two JT distortions at cryogenic temperatures [22]. Finally, we remark that the obtained D_2 symmetry as the global minimum for neutral gold is consistent with the general JT theory and it is compatible with EPR spectroscopy. Indeed, the difference in ground state minima for Au^0 (D_2 distortion) and for its isoelectronic center

Pt^- (C_{2v} configuration) might explain the disparity of EPR signals reported for these centers [21–24].

VI. CONCLUSIONS

In this paper, we have proposed a theoretical framework to understand and predict defect properties, opposite to standard defect-oriented studies. Such framework exploits Group Theory (or JT theory), a symmetry-based toy model and *ab initio* calculations to characterize the APES of common defects in diamond lattices. Starting from the tetrahedral symmetry, we have identified the plausible SB mechanisms, reducing the number of compatible point-group symmetries and hence limiting the possible critical points of the $T \otimes (e + t_2)$ APES. Within our toy model we have characterized the fundamental properties of these JT distortions, including the symmetry of the wave functions and level ordering of defect states. Such detailed symmetry analyze have allowed us to guide the *ab initio* characterization of the APES, by restricting the sampling according to the preserved symmetries. In the case of the reorientation paths, for instance, the reported MEP is found after testing different point-group symmetries as saddle points of the transition.

Treating the vacancy and the Pd, Pt, and Au impurities in silicon as instances of the general $T \otimes (e + t_2)$ JT effect has allowed us to propose theoretical pictures of their APES, which are compliant with the available experimental data. In particular, we have presented a full and quantitative model for the $T_d \rightarrow D_{2d}$ APES in the subspace of two effective coordinates, ultimately proving that transitions between equivalent D_{2d} minima are symmetry protected. We have also sampled instances of the $T_d \rightarrow C_{2v}$ APES, for which no general shape has ever been proposed, by targeting the two MEPs between equivalent distortions. In the particular case of the simple silicon vacancy, we contradict previous theoretical studies that were proposing a C_{3v} symmetry as the saddle point of the reorientation transition at neutral charge state. For the vacancy and the Pd, Pt impurities at negative charge state, we have theoretically proven the existence of two reorientation processes, for which no model had been proposed. Moreover, we have shown that the Pt^- and Au^0 centers have indeed different ground-state configurations, possibly explaining the lack of EPR signal for the latter. To conclude, we emphasize that our resulting pictures are grounded by group theory considerations, overcoming possible numerical biases, and becoming transferable to equivalent systems (e.g., vacancies and substitutional impurities in C, Ge). This paper is therefore of potential technological interest, going from mitigation strategies for the irradiation damage in silicon to the accurate description of electronic excitations in diamond for the realisation of qubits.

[1] G. Wolfowicz, F. J. Heremans, C. P. Anderson, S. Kanai, H. Seo, A. Gali, G. Galli, and D. D. Awschalom, Quantum guidelines for solid-state spin defects, Nat. Rev. Mater. **6**, 906 (2021).

[2] O. Sugino and A. Oshiyama, Electronic structure of the silicon divacancy, Phys. Rev. B **42**, 11869 (1990).

[3] M. Saito and A. Oshiyama, Resonant Bonds in Symmetry-Lowering Distortion Around a Si Divacancy, Phys. Rev. Lett. **73**, 866 (1994).

[4] G. D. Watkins, Comment on "Resonant Bonds in Symmetry-Lowering Distortion Around a Silicon Divacancy", Phys. Rev. Lett. **74**, 4353 (1995).

[5] M. Saito and A. Oshiyama, Saito and Oshiyama Reply:, Phys. Rev. Lett. **74**, 4354 (1995).

[6] H. Seong and L. J. Lewis, First-principles study of the structure and energetics of neutral divacancies in silicon, Phys. Rev. B **53**, 9791 (1996).

[7] M. Pesola, J. von Boehm, S. Pöykkö, and R. M. Nieminen, Spin-density study of the silicon divacancy, Phys. Rev. B **58**, 1106 (1998).

[8] S. Öğüt and J. R. Chelikowsky, Large Pairing Jahn-Teller Distortions Around Divacancies in Crystalline Silicon, Phys. Rev. Lett. **83**, 3852 (1999).

[9] B. Coomer, A. Resende, J. Goss, R. Jones, S. Öberg, and P. Briddon, The divacancy in silicon and diamond, Phys. B: Condens. Matter **273-274**, 520 (1999).

[10] S. Öğüt and J. R. Chelikowsky, *Ab initio* investigation of point defects in bulk Si and Ge using a cluster method, Phys. Rev. B **64**, 245206 (2001).

[11] D. V. Makhov and L. J. Lewis, *Ab initio* study of Jahn-Teller distortions for the divacancy in silicon, Phys. Rev. B **72**, 073306 (2005).

[12] R. R. Wixom and A. F. Wright, Formation energies, binding energies, structure, and electronic transitions of Si divacancies studied by density functional calculations, Phys. Rev. B **74**, 205208 (2006).

[13] J.-i. Iwata, K. Shiraishi, and A. Oshiyama, Large-scale density-functional calculations on silicon divacancies, Phys. Rev. B **77**, 115208 (2008).

[14] H. A. Jahn and E. Teller, Stability of polyatomic molecules in degenerate electronic states - I—Orbital degeneracy, Proc. R. Soc. London **161**, 220 (1937).

[15] G. D. Watkins, An EPR study of the lattice vacancy in silicon, J. Phys. Soc. Jpn. **18**, Suppl II (1962).

[16] Edited by S. T. Pantelides, *Deep Centers in Semiconductors* (Gordon and Breach, Philadelphia, 1992).

[17] C. D. Clark, J. Walker, and R. W. Ditchburn, The neutral vacancy in diamond, Proc. R. Soc. London A **334**, 241 (1973).

[18] W. V. Smith, P. P. Sorokin, I. L. Gelles, and G. J. Lasher, Electron-spin resonance of nitrogen donors in diamond, Phys. Rev. **115**, 1546 (1959).

[19] K. L. Brower, Jahn-Teller-Distorted Nitrogen Donor in Laser-Annealed Silicon, Phys. Rev. Lett. **44**, 1627 (1980).

[20] K. L. Brower, Deep-level nitrogen centers in laser-annealed ion-implanted silicon, Phys. Rev. B **26**, 6040 (1982).

[21] H. H. Woodbury and G. W. Ludwig, Spin resonance of Pd and pt in silicon, Phys. Rev. **126**, 466 (1962).

[22] F. G. Anderson, R. F. Milligan, and G. D. Watkins, Epr investigation of Pt^- in silicon, Phys. Rev. B **45**, 3279 (1992).

[23] G. D. Watkins and P. M. Williams, Vacancy model for substitutional Ni^-, Pd^-, Pt^-, and Au^0 in silicon, Phys. Rev. B **52**, 16575 (1995).

[24] G. D. Watkins, M. Kleverman, A. Thilderkvist, and H. G. Grimmeiss, Structure of Gold in Silicon, Phys. Rev. Lett. **67**, 1149 (1991).

[25] I. Bersuker, *The Jahn-Teller Effect* (Cambridge University Press, Cambridge, 2006).

[26] X. Gonze, F. Jollet, F. Abreu Araujo, D. Adams, B. Amadon, T. Applencourt, C. Audouze, J.-M. Beuken, J. Bieder, A. Bokhanchuk *et al.*, Recent developments in the ABINIT software package, Comput. Phys. Commun. **205**, 106 (2016).

[27] D. R. Hamann, Optimized norm-conserving Vanderbilt pseudopotentials, Phys. Rev. B **88**, 085117 (2013).

[28] J. P. Perdew, K. Burke, and M. Ernzerhof, Generalized Gradient Approximation Made Simple, Phys. Rev. Lett. **77**, 3865 (1996).

[29] G. Henkelman, B. P. Uberuaga, and H. Jónsson, A climbing image nudged elastic band method for finding saddle points and minimum energy paths, J. Chem. Phys. **113**, 9901 (2000).

[30] F. Bruneval, N. Vast, and L. Reining, Effect of self-consistency on quasiparticles in solids, Phys. Rev. B **74**, 045102 (2006).

[31] E. P. Wigner, *Gruppentheorie und ihre anwendung auf die Quantenmechanik der Atomspektren* (Springer, Wiesbaden, 1931).

[32] R. Jotham and S. Kettle, Geometrical consequences of the Jahn-Teller effect, Inorg. Chim. Acta **5**, 183 (1971).

[33] M. J. Puska, S. Pöykkö, M. Pesola, and R. M. Nieminen, Convergence of supercell calculations for point defects in semiconductors: Vacancy in silicon, Phys. Rev. B **58**, 1318 (1998).

[34] S. Öğüt, H. Kim, and J. R. Chelikowsky, *Ab initio* cluster calculations for vacancies in bulk Si, Phys. Rev. B **56**, R11353 (1997).

[35] M. I. J. Probert and M. C. Payne, Improving the convergence of defect calculations in supercells: An *ab initio* study of the neutral silicon vacancy, Phys. Rev. B **67**, 075204 (2003).

[36] F. El-Mellouhi, N. Mousseau, and P. Ordejón, Sampling the diffusion paths of a neutral vacancy in silicon with quantum mechanical calculations, Phys. Rev. B **70**, 205202 (2004).

[37] A. F. Wright, Density-functional-theory calculations for the silicon vacancy, Phys. Rev. B **74**, 165116 (2006).

[38] F. Corsetti and A. A. Mostofi, System-size convergence of point defect properties: The case of the silicon vacancy, Phys. Rev. B **84**, 035209 (2011).

[39] F. Corsetti and A. A. Mostofi, Negative-U properties for substitutional au in Si, Europhys. Lett. **105**, 57006 (2014).

[40] G. Herrero-Saboya, L. Martin-Samos, A. Jay, A. Hemeryck, and N. Richard, A comprehensive theoretical picture of e centers in silicon: From optical properties to vacancy-mediated dopant diffusion, J. Appl. Phys. **127**, 085703 (2020).

[41] A. Resende, R. Jones, S. Öberg, and P. R. Briddon, Calculations of Electrical Levels of Deep Centers: Application to Au-H and Ag-H Defects in Silicon, Phys. Rev. Lett. **82**, 2111 (1999).

[42] H. Köppel and H. Barentzen, *The Jahn-Teller Effect: Fundamentals and Implications for Physics and Chemistry*, Springer Series in Chemical Physics, 97 (Springer-Verlag, Berlin, 2009).